

## Experimental Evidence for a Berry Curvature Quadrupole in an Antiferromagnet

Soumya Sankar<sup>1,\*</sup>, Ruizi Liu<sup>2,\*</sup>, Cheng-Ping Zhang<sup>1,\*</sup>, Qi-Fang Li<sup>3,4,\*</sup>, Caiyun Chen<sup>1,5,\*</sup>, Xue-Jian Gao<sup>1</sup>, Jiangchang Zheng<sup>1</sup>, Yi-Hsin Lin<sup>1</sup>, Kun Qian<sup>2</sup>, Ruo-Peng Yu<sup>1</sup>, Xu Zhang<sup>4</sup>, Zi Yang Meng<sup>4</sup>, Kam Tuen Law<sup>1</sup>, Qiming Shao<sup>1,2,6,7,†</sup> and Berthold Jäck<sup>1,6,‡</sup>

<sup>1</sup>*The Hong Kong University of Science and Technology, Department of Physics, Clear Water Bay, Kowloon, Hong Kong SAR, China*

<sup>2</sup>*The Hong Kong University of Science and Technology, Department of Electronic and Computer, Clear Water Bay, Kowloon, Hong Kong SAR, China*

<sup>3</sup>*The Institute for Solid State Physics, The University of Tokyo, Chiba, Japan*

<sup>4</sup>*Department of Physics and HKU-UCAS Joint Institute of Theoretical and Computational Physics, The University of Hong Kong, Pokfulam Road, Hong Kong SAR, China*

<sup>5</sup>*Institute for Advanced Study, The Hong Kong University of Science and Technology, Clear Water Bay, Kowloon, Hong Kong SAR, China*

<sup>6</sup>*IAS Center for Quantum Technologies, The Hong Kong University of Science and Technology, Clear Water Bay, Kowloon, Hong Kong SAR, China*

<sup>7</sup>*Guangdong-Hong Kong-Macao Joint Laboratory for Intelligent Micro-Nano Optoelectronic Technology, The Hong Kong University of Science and Technology, Hong Kong SAR, China*

 (Received 6 October 2023; revised 27 March 2024; accepted 7 May 2024; published 17 June 2024)

Berry curvature multipoles appearing in topological quantum materials have recently attracted much attention. Their presence can manifest in novel phenomena, such as nonlinear anomalous Hall effects (NLAHE). The notion of Berry curvature multipoles extends our understanding of Berry curvature effects on the material properties. Hence, research on this subject is of fundamental importance and may also enable future applications in energy harvesting and high-frequency technology. It was shown that a Berry curvature dipole can give rise to a second-order NLAHE in materials of low crystalline symmetry. Here, we demonstrate a fundamentally new mechanism for Berry curvature multipoles in antiferromagnets that are supported by the underlying magnetic symmetries. Carrying out electric transport measurements on the kagome antiferromagnet FeSn, we observe a third-order NLAHE, which appears as a transverse voltage response at the third harmonic frequency when a longitudinal ac drive is applied. Interestingly, this NLAHE is strongest at and above room temperature. We combine these measurements with a scaling law analysis, a symmetry analysis, model calculations, first-principle calculations, and magnetic Monte Carlo simulations to show that the observed NLAHE is induced by a Berry curvature quadrupole appearing in the spin-canted state of FeSn. At a practical level, our study establishes NLAHE as a sensitive probe of antiferromagnetic phase transitions in other materials—such as moiré superlattices, two-dimensional van der Waal magnets, and quantum spin liquid candidates, which remain poorly understood to date. More broadly, Berry curvature multipole effects are predicted to exist for 90 magnetic point groups. Hence, our work opens a new research area to study a variety of topological magnetic materials through nonlinear measurement protocols.

DOI: [10.1103/PhysRevX.14.021046](https://doi.org/10.1103/PhysRevX.14.021046)

Subject Areas: Condensed Matter Physics, Magnetism

### I. INTRODUCTION

In materials with topologically nontrivial electronic states, a finite Berry curvature  $\mathbf{\Omega}$  has a profound influence on the electrical, optical, and thermal materials properties [1,2]. Microscopically,  $\mathbf{\Omega}$  is related to the topology of the quantum-mechanical wave function and can be regarded as the momentum space analogue of a magnetic flux density. Hence, a finite  $\mathbf{\Omega}$  can induce an anomalous Hall effect (AHE), which appears as a finite Hall voltage  $V_H$  in electrical transport measurements [3]. The Berry curvature contribution to the Hall effect arises from its momentum space

\*These authors contributed equally to this work.

†To whom all correspondence should be addressed: [eeqshao@ust.hk](mailto:eeqshao@ust.hk)

‡To whom all correspondence should be addressed: [bjack@ust.hk](mailto:bjack@ust.hk)

Published by the American Physical Society under the terms of the [Creative Commons Attribution 4.0 International license](https://creativecommons.org/licenses/by/4.0/). Further distribution of this work must maintain attribution to the author(s) and the published article's title, journal citation, and DOI.

integration over the occupied electronic states  $M \propto \int f_0 \Omega_z d\mathbf{k}$ , where  $f_0$  is the Fermi-Dirac distribution. Effectively, it can be viewed as a Berry curvature monopole  $M \propto \rho_{xy}^{-1}$ . Because of the direct connection between  $\mathbf{\Omega}$  and the Hall resistivity  $\rho_{xy}$ , the AHE plays a key role in the investigation of topological quantum materials, such as Weyl [4,5] and Dirac [6] fermion systems, and the Chern insulating state in the quantized Hall limit [7–9].

It has been recognized that Berry curvature multipole moments—such as dipoles  $D_{\alpha\beta}$  [10,11], quadrupoles  $Q_{\alpha\beta\gamma}$ , hexapoles, and octupoles [12]—can generally exist. These Berry curvature multipoles derive from the momentum space derivatives of  $\mathbf{\Omega}$ , e.g.,  $D_{\alpha\beta} \propto \int f_0 \partial_\alpha \Omega_\beta d\mathbf{k}$  and  $Q_{\alpha\beta\gamma} \propto \int f_0 \partial_\alpha \partial_\beta \Omega_\gamma d\mathbf{k}$ , where  $\alpha, \beta, \gamma$  denote the spatial directions. Finite Berry curvature multipole moments modify the material properties, and their presence can be experimentally detected, for example, through measurements of the nonlinear anomalous Hall effect (NLAHE). Here, multipole moments induce a finite Hall voltage  $V_H^{n\omega}$  at the higher harmonics  $n\omega$  ( $n = 2, 3, \dots$ ) of a longitudinally applied ac current with frequency  $\omega$ . A finite  $M$  permits a first-order response  $V_H^{1\omega}$  when time-reversal symmetry  $\mathcal{T}$  is broken, which is the conventional linear anomalous Hall effect. The breaking of crystalline inversion symmetry  $\mathcal{P}$  [10] can yield a finite  $D_{\alpha\beta}$ , which permits a second-order Hall response  $V_H^{2\omega}$  even when  $\mathcal{T}$  is preserved. This second-order nonlinear Hall effect was initially observed in bilayer  $\text{WTe}_2$  [13], which is nonmagnetic. Interestingly, it has been predicted that the magnetic point group symmetries of antiferromagnetic materials can support higher-order Berry curvature multipole moments—such as quadrupole, hexapole, and octupole moments—which should manifest in NLAHEs up to the fifth order. Note that Berry curvature multipoles do not induce a longitudinal higher order response. Crucially, the origin of these higher order multipole moments is qualitatively different from that of the previously observed Berry curvature dipole moment [10,13–15], which only requires a low crystalline symmetry. To date, experimental evidence for higher-order Berry curvature effects in antiferromagnets is missing.

Here, we report the observation of a Berry curvature quadrupole (BCQ) induced third-order NLAHE in electric transport measurements conducted on the kagome antiferromagnet (AFM) FeSn [16,17]. The observation of this NLAHE is consistent with expectations from our symmetry analysis, as well as tight-binding and *ab initio* calculations that predict the presence of a BCQ in the spin-canted state of FeSn. Interestingly, the observed NLAHE signal is strongest above room temperature and sensitive to the symmetry of the magnetic order parameter. Our scaling analysis in terms of the charge carrier scattering time reveals the intrinsic BCQ origin of the third-order Hall signal.

## II. RESULTS

### A. Epitaxial FeSn films for electrical transport studies

FeSn (space group  $P6/mmm$ ,  $a = 5.2959 \text{ \AA}$ , and  $c = 4.4481 \text{ \AA}$ ) belongs to the family of transition metal-based kagome metals, which has recently attracted much interest, owing to the presence of the kagome-lattice-derived flat bands [18–20], topological electronic states [6,19], and itinerant magnetism [21,22]. FeSn consists of individual  $\text{Fe}_3\text{Sn}$  and stanene layers that are vertically stacked in alternating order along the crystallographic  $c$  axis [Fig. 1(a)]. The iron (Fe) atoms are arranged on a 2D kagome lattice and contribute an approximate  $2\mu_B$  magnetic moment per atom, which originates from the partially filled  $d$  orbitals. Strong intralayer magnetic exchange interactions  $J$  between the spin  $S = 1$  moments lead to in-plane ferromagnetism, whereas an interlayer antiferromagnetic Heisenberg term  $J_C \cong 0.1J$  results in layered A-type antiferromagnetic order along the  $c$  axis with a Néel temperature  $T_N = 365 \text{ K}$  [17,23,24]. Using solid phase epitaxy with a molecular beam epitaxy system [25], we have synthesized 33-nm-thick FeSn thin films, which were shaped into Hall bar devices [Fig. 1(b)] [26]. The high crystalline quality of the films, which nucleate in a single phase, was confirmed using x-ray diffraction, energy-dispersive x-ray spectroscopy, and transmission electron microscopy experiments (Fig. S1) [26]. Measurements of the temperature-dependent longitudinal resistivity  $\rho_{xx}(T)$  demonstrate the film’s metallic character with a residual resistance ratio  $RRR = R(300 \text{ K})/R(2 \text{ K}) = 23.9$  [Fig. 1(c)]. The overall transport characteristics (Fig. S2) agree with previous studies of MBE-grown antiferromagnetic FeSn films [16,25]; the kink in  $\rho_{xx}(T)$  at  $T = 352 \text{ K}$  can be associated with the onset of AFM [27] at  $T_N$ , whose value for thin films was previously found to be slightly smaller compared to that of bulk crystals [25,27]. The comparably high Néel temperature combined with the ability to grow high-quality thin films makes FeSn particularly well suited to study nonlinear topological transport responses at room temperature.

### B. Measurement of anomalous Hall effects at room temperature

We now turn to the measurement of the linear and nonlinear Hall effects. To this end, we apply a longitudinal ac current  $I_x(\omega)$  to the Hall bar device D1 and measure the transverse Hall voltages  $V_{xy}^{1\omega}$ ,  $V_{xy}^{2\omega}$ , and  $V_{xy}^{3\omega}$  via phase-sensitive lock-in detection as a function of an external magnetic field  $B$  applied in the out-of-plane direction at room temperature  $T = 300 \text{ K}$  [Fig. 1(b)]. Control measurements to ensure the accuracy of our lock-in detection method are discussed in Sec. V. In Fig. 1(d), we display the anomalous contribution to the first-order Hall resistivity  $\rho_{\text{AHE}}^{1\omega}(B)$ . Note that  $\rho_{\text{AHE}}^{1\omega}(B)$  can be obtained from the Hall resistivity  $\rho_{xy}^{1\omega}(B)$  by subtracting the linear contribution to

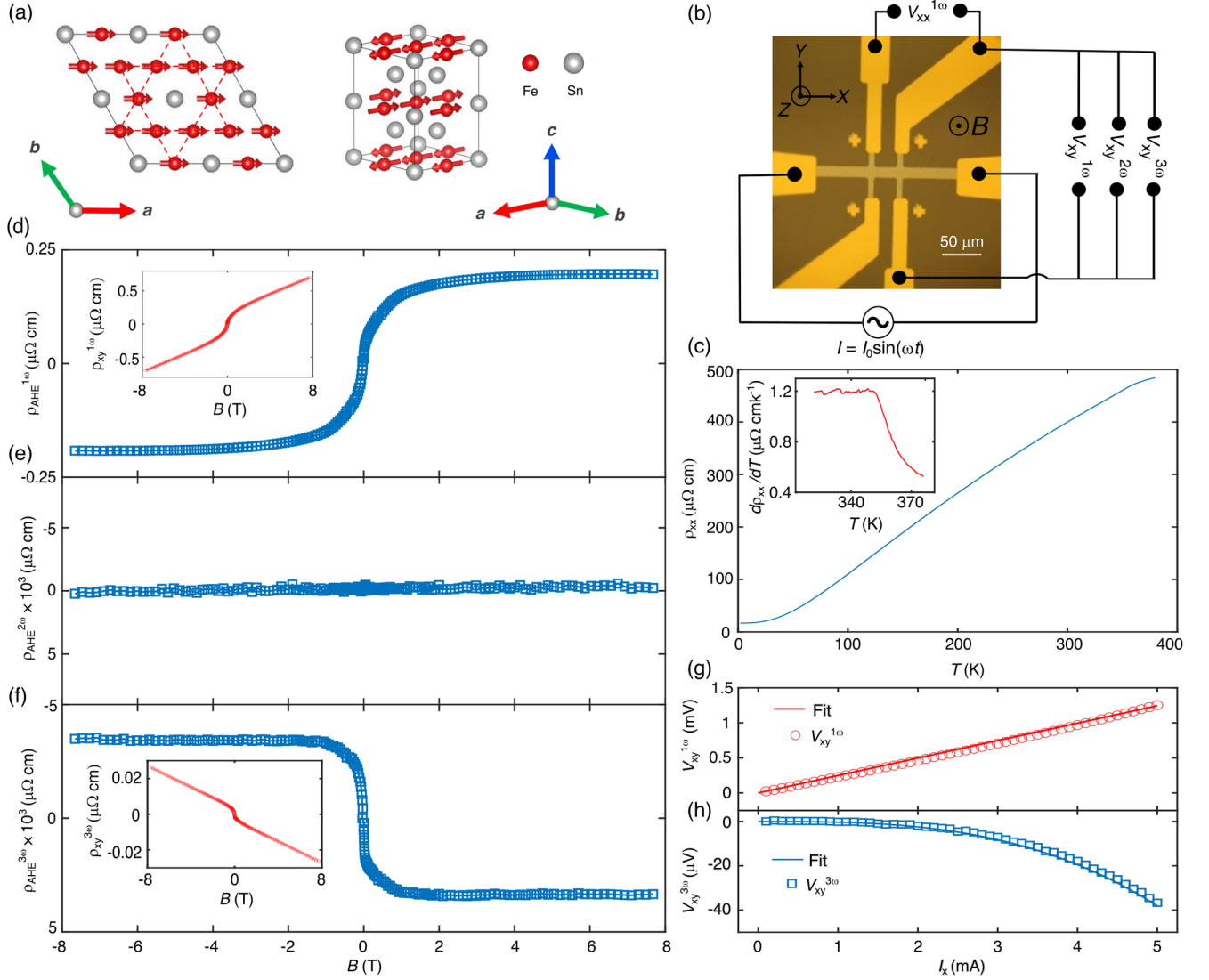


FIG. 1. Room temperature third-order nonlinear anomalous Hall effect in FeSn thin films. (a) Crystallographic and magnetic structure of FeSn forming an A-type antiferromagnet. The iron (Fe) atoms occupy the sites of the kagome lattice that coordinates a triangular tin (Sn) lattice. The vertical stacking of the kagome planes along the  $c$  axis is coordinated by individual stanene spacer layers. (b) Optical micrograph of the Hall bar device and the electrical transport measurement geometry [26]. (c) Measurement of the temperature  $T$ -dependent longitudinal resistivity  $\rho_{xx}(T)$ . The inset displays the corresponding derivative  $d\rho_{xx}(T)/dT$ . (d) Linear  $\rho_{\text{AHE}}^{1\omega}$ , (e) second-order nonlinear  $\rho_{\text{AHE}}^{2\omega}$ , and (f) third-order nonlinear  $\rho_{\text{AHE}}^{3\omega}$  anomalous Hall resistivity as a function of the magnetic field  $B$  measured at  $T = 300$  K. The insets in panels (a) and (f) display the corresponding Hall resistivities  $\rho_{xy}^{1\omega}(B)$  and  $\rho_{xy}^{3\omega}(B)$ , respectively, before the linear background subtraction (see main text). (g) First-order linear  $V_{xy}^{1\omega}$  and (h) third-order nonlinear  $V_{xy}^{3\omega}$  Hall voltages measured as a function of the longitudinal drive current  $I_x$  at  $T = 300$  K and  $B = 8$  T (open symbols). The solid lines show a linear and cubic fit, respectively, to the experimental data.

the Hall effect  $\rho_L^{1\omega}$ ,  $\rho_{\text{AHE}}^{1\omega}(B) = \rho_{xy}^{1\omega}(B) - \rho_L^{1\omega}(B)$  [cf. Fig. 1(d) inset]. Here,  $\rho_L^{1\omega}(B)$  likely contains contributions from the orbital Hall effect  $R_H^{1\omega}$  and (an anomalous part linear in  $B$ ) from the linear magnetic susceptibility of the Fe magnetic moments to the out-of-plane magnetic field  $R_0^{1\omega}$  [17]. We note that their relative contributions to  $\rho_L^{1\omega}$  are difficult to separate unless the out-of-plane magnetization is saturated. The resulting  $\rho_{\text{AHE}}^{1\omega}(B)$  is an odd function of  $B$ , and it saturates at large field values  $|B| > 2$  T. By contrast, we do

not observe a second-order AHE, and  $\rho_{\text{AHE}}^{2\omega}(B)$  fluctuates around zero resistivity [Fig. 1(e)].

On the other hand, we observe a strong third-order Hall response [Fig. 1(f)]. It contains a linear background  $\rho_0^{3\omega}(B)$  as well as an anomalous part  $\rho_{\text{AHE}}^{3\omega}(B)$ , which is nonlinear in  $B$  and which saturates at  $|B| < 2$  T. The third-order anomalous Hall resistivity  $\rho_{\text{AHE}}^{3\omega}(B)$  can be obtained by subtracting  $\rho_0^{3\omega}(B)$  from the third-order Hall resistivity  $\rho_{xy}^{3\omega}(B)$ ,  $\rho_{\text{AHE}}^{3\omega}(B) = \rho_{xy}^{3\omega}(B) - \rho_0^{3\omega}(B)$  [Fig. 2(e) inset].

As we will show below,  $\rho_{\text{AHE}}^{3\omega}(B)$  predominantly arises from the BCQ. On the one hand,  $\rho_0^{3\omega}(B)$  can contain two contributions, first, a magnetic-field-induced third-order orbital Hall effect. This effect likely results from a third-order correction to the longitudinal drift velocity, which gives rise to a Drude-type third-order longitudinal resistivity  $\rho_{\text{xx}}^{3\omega}$  [see Fig. S14(b) for measurements of  $\rho_{\text{xx}}^{3\omega}$  on device D4]. Note that  $\rho_0^{3\omega}(B)$  could also contain contributions from the BCQ, which evolves nearly linearly with  $B$  over large field ranges [see Fig. 3(b) and related discussion of our model calculations]. Because discerning between these two contributions to  $\rho_0^{3\omega}(B)$  is difficult, we will focus our following analysis on  $\rho_{\text{AHE}}^{3\omega}(B)$ , which is free from orbital effects. Like  $\rho_{\text{AHE}}^{\omega}(B)$ ,  $\rho_{\text{AHE}}^{3\omega}(B)$  is an odd function of  $B$ , and it displays  $B$ -independent characteristics at  $|B| \gg 0$  T. We have further studied the dependence of the measured Hall voltages on the longitudinal current drive  $I_x$  at  $B = 8$  T [Figs. 1(g) and 1(h)]. The observed  $V_{\text{xy}}^{1\omega}(I_x) \propto I_x$  and  $V_{\text{xy}}^{3\omega}(I_x) \propto I_x^3$  relations establish the first- and third-order nature of the measured Hall voltages.

### C. Experimental characterization of the Hall effects

To characterize the observed AHEs in more detail, we study their temperature dependence. Consistent with the room-temperature observations, we do not observe a second-order AHE at any temperature (Fig. S3). In Fig. 2(a), we display  $\rho_{\text{AHE}}^{1\omega}(B)$  measured at different temperatures [Figs. S2(a) and S2(b) show the temperature dependence of  $\rho_{\text{xy}}^{1\omega}(B)$  and  $\rho_{\text{xy}}^{3\omega}(B)$ , respectively]. While  $\rho_{\text{AHE}}^{1\omega}(B)$  vanishes for  $T < 90$  K,  $\rho_{\text{AHE}}^{1\omega}(B)$  monotonically increases with increasing temperature and plateaus at  $T > 330$  K. By comparison,  $\rho_{\text{AHE}}^{3\omega}(B)$  shows a much richer temperature response [Fig. 2(b)]. Like  $\rho_{\text{AHE}}^{1\omega}(B)$ ,  $\rho_{\text{AHE}}^{3\omega}(B)$  vanishes at  $T < 90$  K and increases with temperature up to  $T = 330$  K. However,  $\rho_{\text{AHE}}^{3\omega}(B)$  then decreases and exhibits a sign change between 350 and 360 K. This contrasting behavior at  $T > 330$  K is also illustrated in Figs. 2(c) and 2(d), which display the temperature dependence of  $\rho_{\text{AHE}}^{1\omega}|_{B=-4\text{ T}}(T)$  and  $\rho_{\text{AHE}}^{3\omega}|_{B=-4\text{ T}}(T)$  at  $T > 90$  K. Furthermore,  $\rho_{\text{AHE}}^{1\omega}(B)$  and  $\rho_{\text{AHE}}^{3\omega}(B)$  sensitively depend on the spatial orientation of  $B$  with respect to the crystallographic axes of FeSn. When  $B$

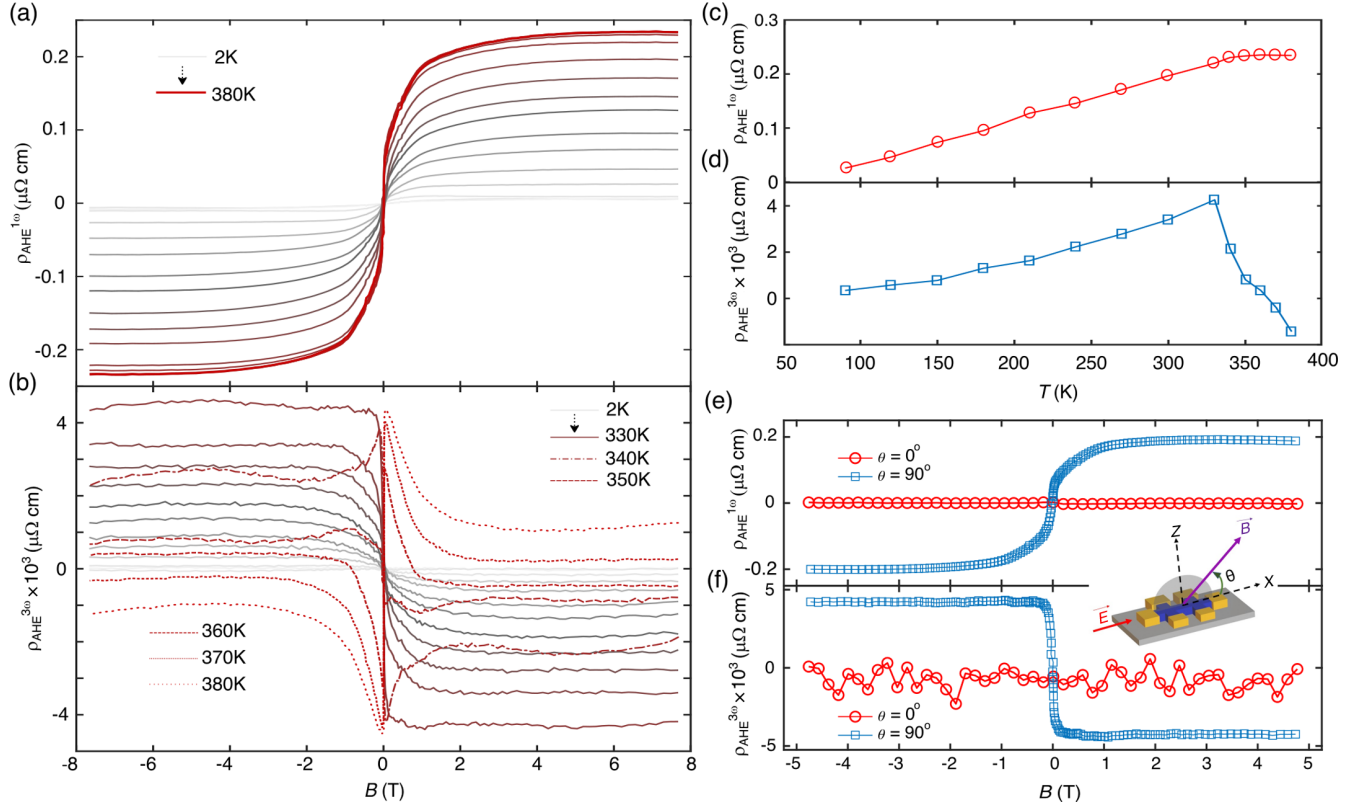


FIG. 2. Experimental characterization of the linear and nonlinear anomalous Hall effects. (a) Linear  $\rho_{\text{AHE}}^{1\omega}$  and (b) third-order nonlinear  $\rho_{\text{AHE}}^{3\omega}$  anomalous Hall resistivities as a function of the magnetic field  $B$  measured at different temperatures  $T$ . (c)  $\rho_{\text{AHE}}^{1\omega}$  and (d)  $\rho_{\text{AHE}}^{3\omega}$  at  $B = -4$  T plotted as a function of  $T$ . (e)  $\rho_{\text{AHE}}^{1\omega}(B)$  and (f)  $\rho_{\text{AHE}}^{3\omega}(B)$  measured at different spatial orientations of  $B$  with respect to the longitudinal Hall bar axis  $X$ . At  $\theta = 0^\circ$ ,  $B$  is aligned in parallel to  $X$ , and at  $\theta = 90^\circ$ ,  $B$  is aligned perpendicular to  $X$  in the out-of-plane direction that is parallel to the crystallographic  $c$  axis. In all measurements, the current bias  $I_x$  is applied along the  $X$  direction.

lies within the crystallographic  $a - b$  plane, both  $\rho_{\text{AHE}}^{1\omega}(B)$  and  $\rho_{\text{AHE}}^{3\omega}(B)$  vanish in measurements conducted at  $T = 300$  K [see Figs. 2(e) and 2(f); measurements at other temperatures are shown in Fig. S4]. This concludes the main experimental results of our work, demonstrating the third-order NLAHE over a wide temperature window extending beyond room temperature (see Figs. S5, S6, and S14 for measurements of other Hall bar devices D2, D3, and D4, respectively). The observed third-order NLAHE in our study is an odd function of the magnetic field. Therefore, it must have a different origin than the Berry curvature dipole and Berry connection polarizability-induced second- and third-order nonlinear Hall effects [10,28], which are an even function of the magnetic field; i.e., they are finite at zero magnetic field when  $\mathcal{T}$  is intact. In the following, we show that our observations are consistent with a  $Q_{\alpha\beta\gamma}$ -induced third-order NLAHE in an A-type kagome antiferromagnet whose spins are canted toward the  $c$  axis.

#### D. Symmetry analysis and electronic structure calculations

First, we illustrate this concept by considering the magnetic structure of FeSn [Fig. 1(a)], which belongs to the magnetic point group  $mmm1'$ . The presence of finite Berry curvature moments follows from a symmetry analysis. Because  $mmm1'$  preserves  $\mathcal{P} \cdot \mathcal{T}$ , native FeSn does not exhibit a  $\Omega$ -induced AHE. On the other hand, canting of the spins toward the  $c$  axis, such as induced by an externally applied magnetic field, lowers the symmetry to  $2/m$ , which breaks  $\mathcal{P} \cdot \mathcal{T}$  and permits a finite  $M$  and  $Q_{\alpha\beta\gamma}$ , while  $D_{\alpha\beta}$  vanishes. Hence, an A-type kagome AFM with spin canting along the  $c$  axis is expected to exhibit a first- and third-order AHE, whereas the second-order AHE is zero. To support this hypothesis, we set up a corresponding nearest-neighbor tight-binding model with spin-orbit coupling and spin canting  $M_z$  [26,29]. This model allows us to qualitatively determine Berry curvature-related contributions to the linear and third-order NLAHE. Figures 3(a) and 3(b) display  $M$  and  $Q_{\text{xxz}}$ , respectively, as a function of the out-of-plane spin canting  $M_z$ . We find  $M = Q_{\text{xxz}} = 0$  if  $M_z = 0$  ( $\mathcal{P} \cdot \mathcal{T}$  preserved), consistent with results from our measurements in which the magnetic field is applied along the Hall bar direction [cf. Figs. 2(e) and 2(f)]. On the other hand,  $M$  and  $Q_{\text{xxz}}$  are finite if  $M_z \neq 0$  ( $\mathcal{P} \cdot \mathcal{T}$  broken). The underlying  $\Omega$  primarily originates from the massive Dirac cones at the  $K$  points in the electronic structure (see Fig. S7). Even in the absence of AFM at  $T > T_N$ ,  $M_z \neq 0$  breaks  $\mathcal{T}$  and results in  $M$ ,  $Q_{\text{xxz}} \neq 0$  [see Figs. 3(c) and 3(d)]. Notably,  $Q_{\text{xxz}}$  changes sign at the transition from a canted antiferromagnetic to a canted paramagnetic phase at  $T_N$ . While not dictated by symmetry, this sign change highlights the sensitivity of  $Q_{\text{xxz}}$  to the underlying magnetic and electronic material properties [30]. Importantly, our calculations further show that  $M$  and  $Q_{\text{xxz}}$  can generally exhibit a nonlinear dependence on  $M_z$  both in the para- and

antiferromagnetic phases [Figs. 3(a)–3(d)]. The detailed relation between  $M$  and  $Q_{\text{xxz}}$  and  $M_z$  is influenced by the details of the underlying electronic band structure. Even though  $M_z \propto B$  was found in previous magnetometry studies of FeSn [17], the first- and third-order Hall responses can contain anomalous contributions that are not linear in  $B$ , as observed in our measurements [cf. Figs. 1(d) and 1(f)].

This supposition is largely consistent with results from *ab initio* calculations of the electronic structure of FeSn [26]. The band structure of our density functional theory (DFT)-derived Wannier Hamiltonian in the antiferromagnetic phase (see Fig. S9) is characterized by a complex Fermi surface with multiple electron and hole pockets [see Figs. 4(a) and 4(b) insets for the calculated Fermi surfaces]. We include a canting term  $M_z$  to simulate the spin canting along the  $c$  axis. At  $M_z \neq 0$ , the double band degeneracy in both the antiferromagnetic ( $T < T_N$ ) and paramagnetic ( $T > T_N$ ) states is lifted and indeed yields finite  $M$  and  $Q_{\text{xxz}}$  in the antiferromagnetic [Figs. 4(a) and 4(b)] and paramagnetic phases, respectively [26]. As can be seen,  $M$  and  $Q_{\text{xxz}}$  deviate from a strictly linear dependence on  $M_z$ . Especially in the limit  $M_z \rightarrow 0$ , symmetry-breaking effects could have an outsized effect on the generation of  $M$  and  $Q_{\text{xxz}}$  in the complex electronic band structure of FeSn. This finding is consistent with the observation of anomalous contributions  $\rho_{\text{AHE}}^{1\omega}$  and  $\rho_{\text{AHE}}^{3\omega}$  to the Hall response at  $|B| < 2$  T. Overall, the results of the symmetry analysis, tight-binding model, and the electronic structure calculation support a  $Q_{\text{xxz}}$ -induced third-order NLAHE.

#### E. Spin-canted state of FeSn

The spin-canted state of FeSn with a finite  $c$ -axis magnetization ( $\sim 0.01 \mu_B/\text{Fe}$  atom) in the presence of an out-of-plane magnetic field was previously established by magnetometry measurements over a wide temperature window (2 K to 300 K) [17]. Here, we use classical Monte Carlo simulations based on realistic magnetic exchange terms of FeSn [17] to further demonstrate that this canted state results from the interplay between critical thermal fluctuations near  $T_N$  and an externally applied magnetic field [26]. The resulting in-plane  $\langle M_{xy}(0, 0, \pi)^2 \rangle$  and out-of-plane  $\langle M_z^2 \rangle$  spin correlation functions are shown in Figs. 4(c) and 4(d), respectively. At  $T \ll T_N$ , the Fe spins lie almost parallel to the  $a-b$  plane owing to a finite easy-plane crystalline anisotropy, and they exhibit A-type AFM order [cf. Fig. 1(a)]. As temperature increases, thermal fluctuations gradually weaken this magnetic order and  $\langle M_{xy}(0, 0, \pi)^2 \rangle \rightarrow 0$  near  $T_N = 0.76J_{\parallel}$ , which is consistent with the reported  $T_N$  [17]. This “thermal softening” of the in-plane spin alignment permits a finite out-of-plane spin canting  $\langle M_z^2 \rangle > 0$  in the presence of an out-of-plane magnetic field. This effect is the strongest near  $T_N$  at which critical fluctuations render the spins extremely

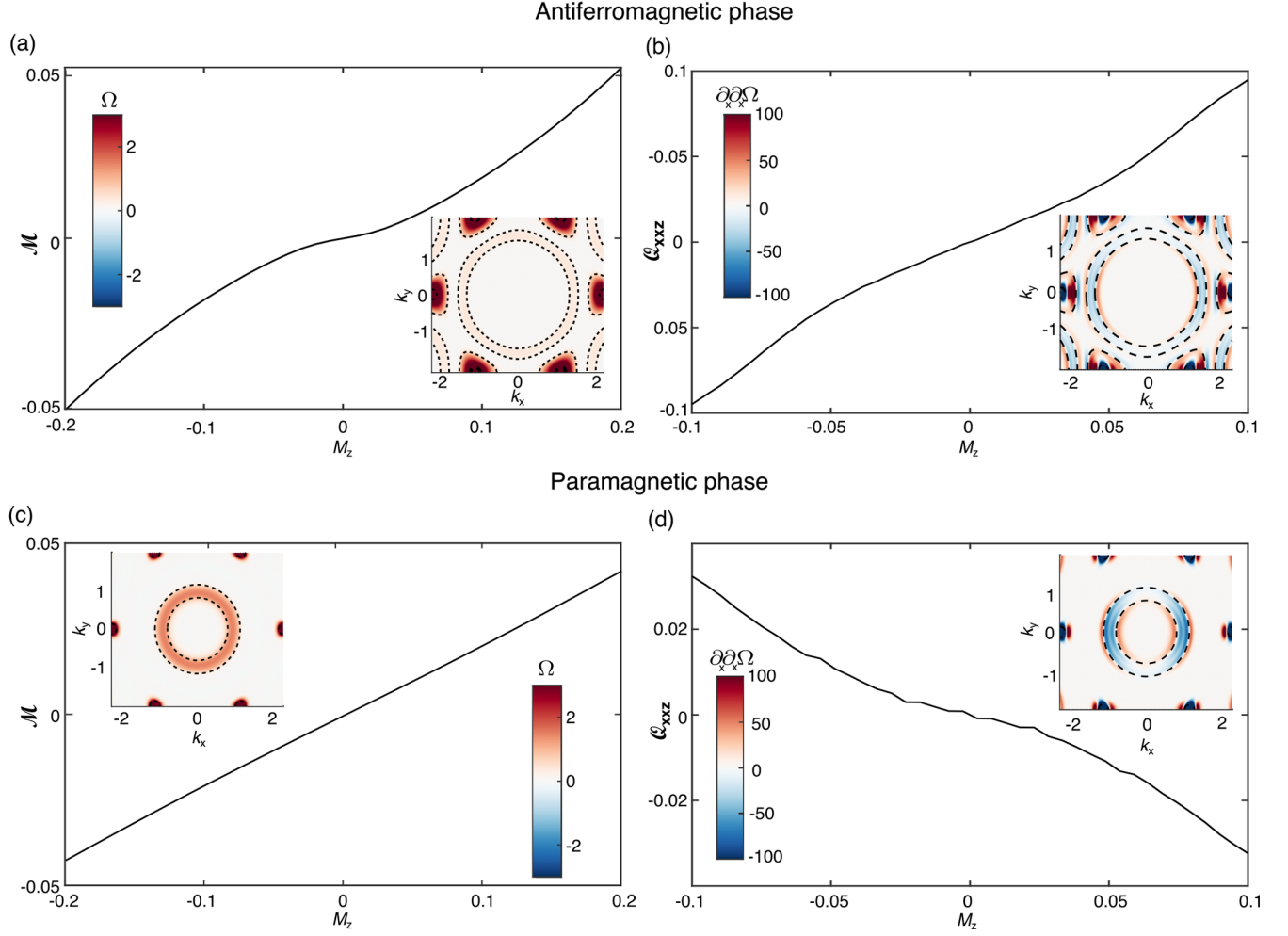


FIG. 3. Berry curvature quadrupole of an A-type antiferromagnet on the kagome lattice with canted spins in the antiferromagnetic and paramagnetic phases. (a) Berry curvature monopole  $M$  and (b) Berry curvature quadrupole  $Q_{xxx}$  of an A-type kagome antiferromagnet as a function of an out-of-plane magnetization  $M_z$ , owing to spin canting, as calculated from a tight-binding lattice model. The corresponding momentum  $k_{x,y}$ -dependent Berry curvature  $\Omega$  and spatial derivative  $\partial_x \partial_x \Omega$  are shown in the insets. (c)  $M$  and (d)  $Q_{xxx}$  of the canted kagome paramagnet as a function of  $M_z$ . The corresponding momentum  $k_{x,y}$ -dependent  $\Omega$  and  $\partial_x \partial_x \Omega$  are shown in the respective insets. See main text and Ref. [26] for model details.

susceptible to external perturbations, in this case, the out-of-plane magnetic field. Therefore,  $\langle M_z^2 \rangle$  gradually increases with temperature, peaks at  $T_N$ , and remains finite even at  $T > T_N$ . Magnetic-field-dependent simulations further confirm the linear susceptibility and magnitude of the previously experimentally determined out-of-plane magnetization (Fig. S10) [17]. Overall, these characteristics are consistent with our experimental observations of the first- and third-order AHE, both of which require an out-of-plane spin-canted state to take finite values:  $\rho_{\text{AHE}}^{1\omega}$  and  $\rho_{\text{AHE}}^{3\omega}$  vanish at  $B = 0$  T and  $T \rightarrow 0$  K, exhibit a monotonic growth toward  $T_N$  in a finite out-of-plane magnetic field, and remain finite at  $T > T_N$  and  $B \neq 0$  T. We note that the residual  $\langle M_z^2 \rangle$  at  $B = 2$  T and  $T = 0$  K could be too small to induce a measurable AHE. Possible spin-charge interactions [17] and quantum-mechanical corrections could

further amend the low-temperature magnetic structure via second-order effects not considered in our model.

### III. DISCUSSION

#### A. Excluding competing mechanisms

It is important to distinguish intrinsic  $Q_{xxx}$  contributions to  $\rho_{\text{AHE}}^{3\omega}$  from possible extrinsic contributions. In general, extrinsic contributions to the third-order Hall response can result from impurity scattering [31–33], a longitudinal Drude response [see Fig. S14 for measurements of  $\rho_{xx}^{3\omega}(T)$  on device D4], and Joule heating [34,35]. In the presence of an external magnetic field applied in the out-of-plane direction,  $\rho_{xx}^{3\omega}$  results in a third-order orbital Hall effect that contributes to the linear background  $\rho_0^{3\omega}(B)$  of the Hall response  $\rho_{xy}^{3\omega}$ . As such, neither the third-order

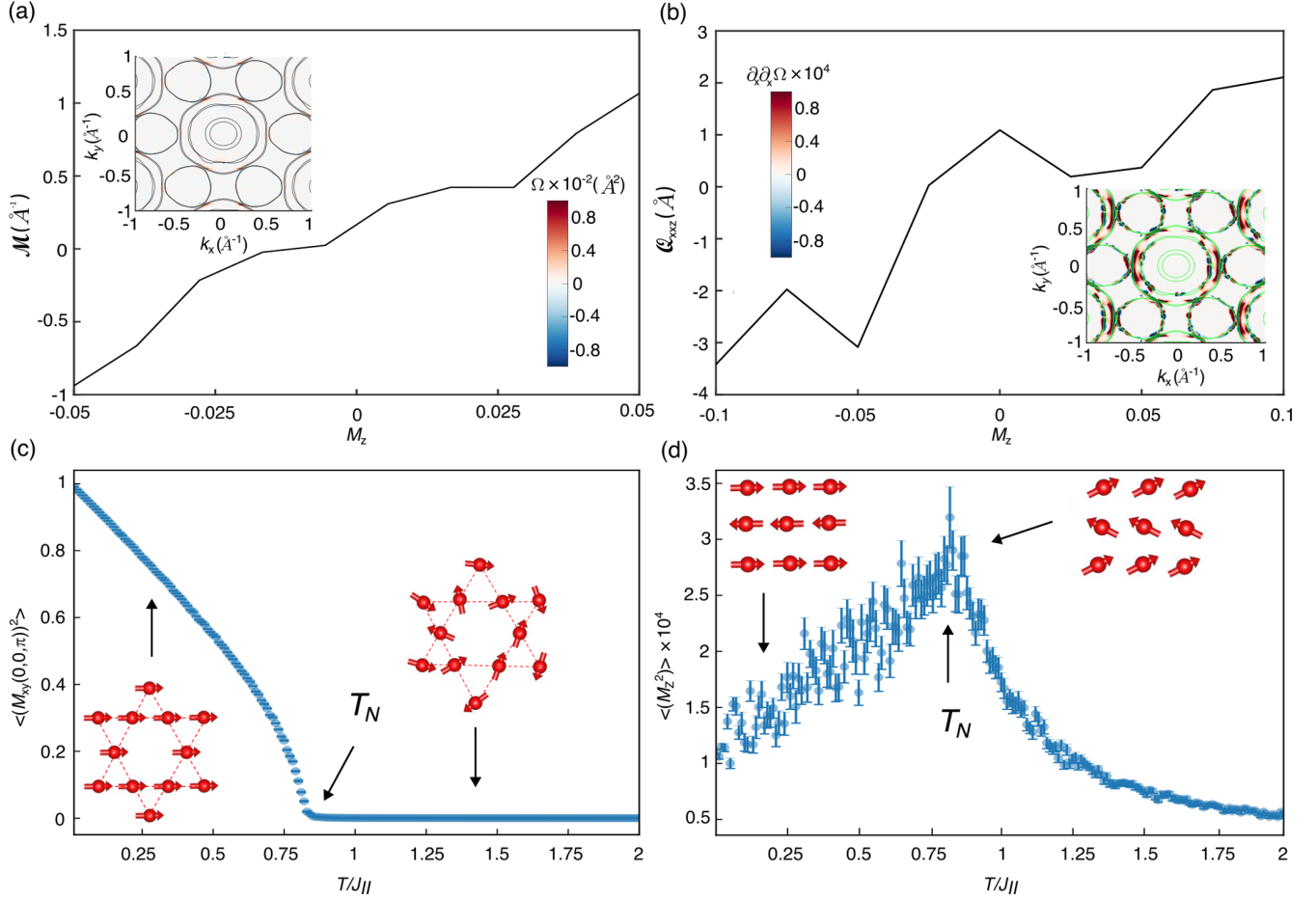


FIG. 4. Berry curvature monopole and quadrupole in the spin-canted state of FeSn. (a) Berry curvature monopole  $M$  as a function of the out-of-plane spin canting  $M_z$ , calculated from the DFT-derived electronic structure of FeSn [16,26]. The inset displays the corresponding momentum  $k_{x,y}$ -dependent Berry curvature  $\Omega$  distribution at Fermi energy ( $M_z = 0.05$ ). (b) Corresponding Berry curvature quadrupole  $Q_{xxz}$  as a function of  $M_z$ . The inset displays the corresponding  $k_{x,y}$ -dependent second derivative  $\partial_x^2 \Omega$  at Fermi energy, and the Fermi surface is depicted as a green line. (c) In-plane  $\langle M_{xy}(0,0,\pi)^2 \rangle$  and (d) out-of-plane  $\langle M_z^2 \rangle$  spin correlations as a function of temperature  $T$  in the presence of an external magnetic field  $B = 2$  T applied along the crystallographic  $c$  axis as obtained from magnetic Monte Carlo simulations [26]. Note that  $T$  is parametrized in terms of the ferromagnetic in-plane exchange  $J_{||}$ . The insets in panel (a) schematically display the corresponding in-plane spin-polarization, both in the ordered state near  $T = 0$  K and above Néel temperature  $T_N$  when in-plane spin correlations vanish. The insets in panel (b) schematically display the corresponding out-of-plane spin polarization at  $T \ll T_N$  when spin canting is weak and at  $T \leq T_N$  when the canting effect is maximum.

Drude response nor Joule heating can account for the observed  $\rho_{\text{AHE}}^{3\omega}$ .

To further distinguish between  $Q_{xxz}$  and skew scattering contributions to  $\rho_{\text{AHE}}^{3\omega}$ , we developed a scaling law analysis for the third-order NLAHE in terms of the charge carrier scattering time  $\tau$  [13,14,26,36]. BCQ contributions to the third-order Hall effect are predicted to scale as  $\tau^2$ . By contrast, skew scattering contributions to the third-order Hall effect are predicted to scale as  $\tau^4$  [26]. The scaling behavior of the experimentally observed third-order Hall effect can be analyzed through the temperature dependence of the anomalous Hall ( $E_{\text{AHE}}^{3\omega}$ ) and longitudinal ( $E_{xx}$ ) electric field ratio  $E_{\text{AHE}}^{3\omega}/E_{xx}^3$  and the longitudinal conductivity  $\sigma_{xx}$  at  $T < T_N$  [Fig. 5(a)] [26]. Above  $T = 200$  K, we

find that  $E_{\text{AHE}}^{3\omega}/E_{xx}^3$  is nearly temperature independent, a characteristic that is typically associated with intrinsic Berry curvature-related contributions to the Hall effect. The scattering time dependence can then be parametrized as  $E_{\text{AHE}}^{3\omega}/(E_{xx}^3 \sigma_{xx}) = \alpha \sigma_{xx}^2 + \beta$ , where  $\alpha$  accounts for skew scattering and  $\beta = (m_{\text{eff}}^2/2\hbar^3 n^2) Q_{xxz}$  for the intrinsic BCQ contribution [36] ( $m_{\text{eff}}$  denotes the effective electron mass,  $\hbar$  the reduced Planck's constant, and  $n$  the charge carrier density). The intrinsic BCQ-related contribution dominates the Hall response in the limit  $\sigma_{xx}^2 \rightarrow 0$  and is proportional to the vertical intercept  $\beta$ . Indeed, our corresponding analysis [Fig. 5(b)] demonstrates that the experimentally observed third-order anomalous Hall effect satisfies the derived scaling law. The significant amplitude of the vertical

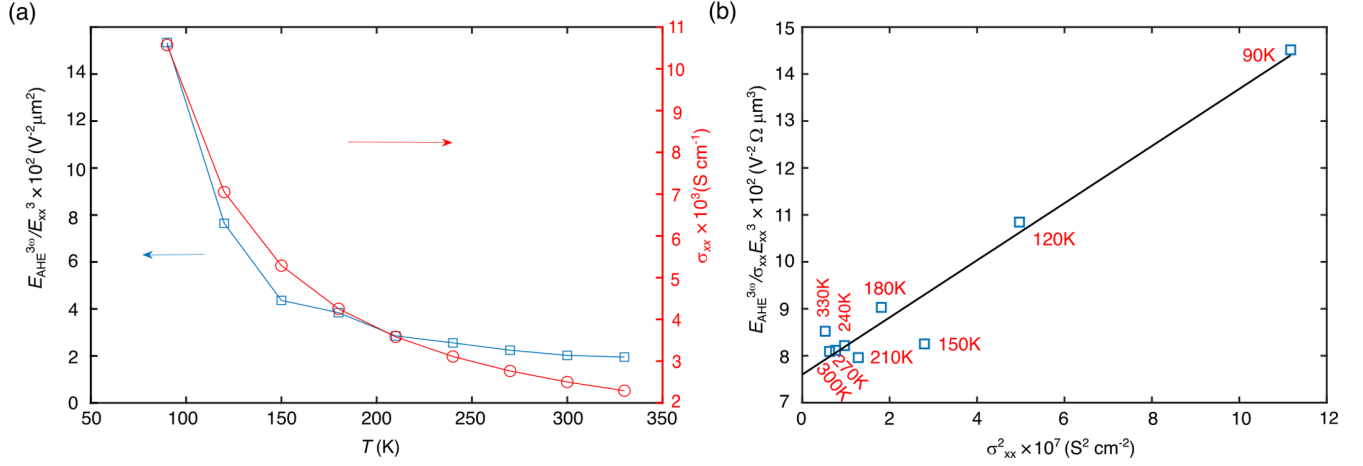


FIG. 5. Scaling law analysis of the third-order nonlinear AHE. (a) Ratio of the AHE electric field  $E_{\text{AHE}}^{3\omega}$  and the cubed longitudinal electric field  $E_{xx}$  (left axis), and longitudinal conductivity  $\sigma_{xx}$  (right axis) as a function of  $T$ . Here,  $E_{\text{AHE}}^{3\omega} = V_{\text{AHE}}^{3\omega}/L_{xy}$  with  $L_{xy} \cong 21 \mu\text{m}$ , and  $E_{xx} = V_{xx}/L_{xx}$  with  $L_{xx} \cong 26 \mu\text{m}$ . (b)  $E_{\text{AHE}}^{3\omega}/(\sigma_{xx} E_{xx}^3)$  and fit to the data (solid line) plotted as a function of  $\sigma_{xx}^2$ . The respective temperatures associated with the data points are indicated.

intercept at  $\sigma_{xx}^2 \rightarrow 0$  indicates that intrinsic contributions dominate over a wide temperature range (approximately 95% at  $T = 300 \text{ K}$ ), while skew scattering only becomes relevant at  $T < 100 \text{ K}$ . This finding distinguishes our results from existing work on nonlinear Hall effects in which the relative contribution of the topological transport response to the AHE is much smaller owing to the prevalence of skew scattering [14,37]. Importantly, our analysis is also consistent with the predicted  $\tau^4$  scaling of the skew scattering contribution to the third-order anomalous Hall effect. In passing, we note that contributions to the orbital Hall effect arising from a third-order Drude response and Joule heating also scale as  $\tau^4$  and, as such, would contribute to  $\alpha$ .

Using  $\beta = (7.6 \pm 0.2) \times 10^2 \Omega \mu\text{m}^3 \text{V}^{-2}$  obtained from fitting  $E_{\text{AHE}}^{3\omega}/(E_{xx}^3 \sigma_{xx})$ ,  $m_{\text{eff}} = 5.4 m_e$  [16] ( $m_e$  denotes the electron mass), and  $n = 1 \times 10^{21} \text{ cm}^{-3}$  (from density functional theory calculations [26]), we obtain  $Q_{\text{xxz,exp}} = 73 \pm 2 \text{ \AA}$ . We note that the equivalent scaling analysis [36] of the first-order AHE (Fig. S8) also suggests an intrinsic origin of  $\rho_{\text{AHE}}^{1\omega}$ , consistent with our expectation from the symmetry analysis, tight-binding model, and electronic structure calculations. Here,  $Q_{\text{xxz,exp}}$  deviates from  $Q_{\text{xxz,calc}} \sim 10^0 \text{ \AA}$ , which can be obtained from the DFT-derived Wannier states (Fig. S9). This deviation can have multiple origins. First, the accuracy of DFT to approximate the complex electronic structure of FeSn is generally limited, which makes a quantitative estimate based on DFT less reliable. Second, the narrow  $\Omega$  and  $\partial_x \partial_x \Omega$  distributions [cf. Figs. 4(a) and 4(b)] in momentum space render a quantitative estimate of  $Q_{\text{xxz,calc}}$  inherently challenging [26]. Moreover, uncertainties in the actual  $m_{\text{eff}}$  [16], as well as an impurity-induced reduction of  $n$ , could further influence the  $Q_{\text{xxz,exp}}$  magnitude [26]. We note that

the FeSn films contain a crystallographic subdomain that is rotated by  $\Delta\phi = 30^\circ$  in the film plane (see Fig. S1). The underlying  $2/m$  symmetry should result in a twofold symmetry of the  $Q_{\text{xxz}}$ -induced third-order Hall response when the longitudinal current  $I_x(\omega)$  is applied parallel or antiparallel to the AFM-order parameter within the crystallographic  $ab$  plane. The presence of domains breaks this symmetry, and the other quadrupole component  $Q_{\text{yyz}}$  comes into play. In this case, the associated nonlinear Hall signal is expected to be more isotropic, containing  $Q_{\text{xxz}}$  and  $Q_{\text{yyz}}$  contributions. In our study, the effective amplitude of  $\rho_{\text{AHE}}^{3\omega}$  thus reflects the underlying domain structure.

Finally, while the multiband Fermi surface of FeSn [Figs. 4(a) and 4(b) insets] could generally contribute to an S-shaped Hall response [Fig. 1(f)], the derived scaling law is robust against multiband transport [26]. Hence, based on the presented scaling analysis, we can exclude multiband transport as a possible origin of the observed third-order NLAHE. Because we are not aware of other mechanisms that can give rise to a third-order Hall signal with these scaling characteristics, our analysis strongly supports the Berry curvature quadrupole origin of the observed third-order NLAHE.

#### IV. CONCLUSION

Our study presents experimental evidence for the Berry curvature quadrupole-induced third-order NLAHE at room temperature in spin-canted FeSn [12,30]. This conclusion is supported by a scaling law analysis, a symmetry analysis, model calculations, first-principle calculations, and magnetic Monte Carlo simulations whose results are consistent with the experimentally observed phenomenology. Hence, our work suggests that Berry curvature multipoles can be

supported by the magnetic point group symmetries of antiferromagnets. This finding constitutes a fundamentally new mechanism for the NLAHE ( $\mathcal{T}$  broken,  $\mathcal{P}$  preserved) which is qualitatively distinct from the Berry curvature dipole ( $\mathcal{T}$  preserved,  $\mathcal{P}$  broken) [13,14] and the quantum metric dipole (product preserved) [38,39] induced second-order NLAHEs by symmetry arguments. Because Berry curvature multipoles are predicted to exist for 90 magnetic point groups [12], our work opens a new field to study a variety of magnetic materials, whose topological electronic states were previously inaccessible, through nonlinear measurement protocols. Of particular interest will be materials in which Berry curvature multipoles are predicted to appear in the leading order [12], such as a BCQ in antiferromagnetic SrMnBi<sub>2</sub> thin films with broken inversion symmetry (magnetic point group  $4'm'm$ ) [40] and a Berry curvature hexapole in the noncollinear antiferromagnet TbAuIn (magnetic point group  $\bar{6}1'$ ) [41]. Owing to the observed sensitivity of the third-order NLAHE to the electronic and magnetic material properties [12,30], our work showcases the use of NLAHEs as a sensitive electric transport probe to investigate antiferromagnetic phase transitions of various materials—such as moiré superlattices [42], two-dimensional van der Waal magnets [43], quantum spin liquid materials [44,45], and altermagnets [46]—that remain poorly understood to date and that are notoriously difficult to study by using electric transport measurements. Our work further extends previous research on AHEs in antiferromagnets [47–49] to the nonlinear transport regime and highlights antiferromagnets [50–52] as promising candidates to exhibit useful quantum properties at room temperature, owing to comparably large antiferromagnetic exchange terms, the absence of a large net magnetization, and the rich magnetic symmetries. In this regard, the observation of the third-order NLAHE in an epitaxially grown kagome magnet [25,53,54] in our study narrows the gap toward the technological use of nonlinear Hall effects in high-frequency and energy-harvesting applications [55].

## V. METHODS

### A. Sample preparation

Epitaxial FeSn thin films were grown on SrTiO<sub>3</sub> (STO) substrates in the (111) direction (from CrysTec GmbH) by using a home-built molecular beam epitaxy (MBE) setup. The as-received STO (111) substrates were cleaned using sonication in acetone and isopropyl alcohol (IPA) for 5 min each. Single-terminated STO (111) surfaces were obtained by using a hot water etching step performed at 90 °C for 90 minutes. Thermal annealing of the STO (111) substrates was performed at 1050 °C with an oxygen flow of 50 sccm inside a tube furnace for 1 hour. Prior to the thin-film growth, substrates were outgassed inside the MBE chamber at 600 °C at a base pressure of less than  $5 \times 10^{-10}$  mbar. Following the

growth recipe of Inoue *et al.* [25], high-purity Fe (99.99%) and Sn (99.99%) (Alfra Aesar) were co-evaporated from Knudsen effusion cells at a beam flux ratio of 1:2.2 at an approximate growth rate of 1 nm/min to obtain a 30-nm-thick amorphous FeSn film. During the deposition, the STO (111) substrate was held at  $T = 200$  °C. Next, the films were capped with an approximately 6-nm-thick layer of amorphous BaF<sub>2</sub>. FeSn of high crystalline quality were obtained by *in situ* postannealing of the deposited FeSn layer at  $T = 500$  °C using a ramp rate of 5 °C/min during the heat-up and cooldown phase. The FeSn thin films were patterned into six terminal Hall bars [Fig. 1(b)] by using Ar<sup>+</sup> ion milling and optical UV lithography. During the whole fabrication process, the FeSn films were protected by the BaF<sub>2</sub> capping layer. Electrical contacts to the FeSn Hall bar structure were fabricated by evaporating 5-nm/100-nm titanium/gold electrodes. We note that cleaved [56] and argon ion-irradiated [57] STO (111) surfaces can exhibit conducting two-dimensional electron gases at the substrate surface. Neither prepared STO substrates prior to FeSn deposition nor STO substrates after argon ion milling of the Hall bar structures exhibited a finite conductance across the substrate surface in four-probe measurements conducted at ambient conditions. This finding indicates the absence of substrate surface effects in our electric transport measurements.

### B. Electric transport measurements

All transport measurements were carried out in a commercial cryogenic magnet system (J4804 from Cryogenic Limited) using a four-probe contact geometry. The Hall bar devices were wire bonded with 40- $\mu$ m aluminum wire to the chip carrier. Two-terminal measurements between different contact pairs were carried out to ensure Ohmic device contacts (Fig. S11). An ac drive of  $I_x(\omega) = I_0 \sin(\omega t)$  with a peak amplitude peak of  $I_0 = 5$  mA at a frequency of  $f = (\omega/2\pi) = 19.357$  Hz was applied by using a source meter (6221A from Keithley). For dc measurements, an  $I_x = 100$   $\mu$ A dc bias was applied. Four SR830 (Stanford Research Systems) lock-in amplifiers, which were phase matched to the  $I_x$  output, were used to simultaneously measure  $V_{xx}^{1\omega}$ ,  $V_{xy}^{1\omega}$ ,  $V_{xy}^{2\omega}$ , and  $V_{xy}^{3\omega}$  [Fig. 1(b)]. Both  $V_{xy}^{\omega}$  and  $V_{xy}^{3\omega}$  are in phase with the drive frequency, whereas  $V_{xy}^{2\omega}$  is out of phase by  $\pi/2$  with respect to the drive frequency. The lock-in phase was calibrated and monitored for each measurement. Typical phase data of  $V_{xy}^{\omega}$  and  $V_{xy}^{3\omega}$  are shown in Fig. S12. Measurements of  $V_{xy}^{1\omega}$  were conducted using different filters, which have different roll-off characteristics, to ensure the spectral purity of the measured lock-in signals (see Fig. S13). Before any data analysis presented in the main text was conducted, zero-field constant voltage offsets were removed from  $V_{xy}^{\omega}$ ,  $V_{xy}^{2\omega}$ , and  $V_{xy}^{3\omega}$ . These offsets likely arose from a slight misalignment between the FeSn Hall bar and the electrodes, causing a finite albeit small coupling of the longitudinal signal into the Hall voltages.

The zero-field offset Hall signal was found to exhibit random values across different devices. The longitudinal  $\rho_{xx}^{1\omega} = (dL_{xy}/L_{xx})(V_{xx}^{1\omega}/I_x)$  and first- and third-order Hall  $\rho_{xy}^{1\omega,3\omega} = (dL_{xx}/L_{xy})(V_{xx}^{1\omega,3\omega}/I_x)$  resistivities were obtained by considering the film thickness  $d = 30$  nm and Hall bar dimensions  $L_{xx} = 26$   $\mu\text{m}$  and  $L_{xy} = 21$   $\mu\text{m}$ .

### ACKNOWLEDGMENTS

We acknowledge fruitful discussions with Xi Dai, Junwei Liu, and Hisashi Inoue. We appreciate the support of Hui Li, Chenjie Zhou, Jiannong Wang, and Wilwin at an early stage of this project. This work was primarily supported by the Hong Kong RGC (No. 26304221 and No. C6033-22G, B.J.) and the Croucher Foundation (B.J.), the National Key R&D Program of China (Grant No. 2021YFA1401500—R.L., K.Q., and Q.S), and the Hong Kong RGC (Grants No. 17301420, No. 17301721, No. AoE/P-701/20, No. 17309822, and No. A\_HKU703/22—Z.Y.M.). Furthermore, B.J. acknowledges financial support by the start-up fund of the Hong Kong University of Science and Technology, Z.Y.M. acknowledges the K. C. Wong Education Foundation (Grant No. GJTD-2020-01), and K. T. L. acknowledges the support of The Ministry of Science and Technology, China and HKRGC through Grants No. 2020YFA0309601, No. RFS2021-6S03, No. C6025-19G, No. AoE/P-701/20, No. 16310520, and No. 16310219. Q.-F.L. acknowledges financial support from the MERIT-WINGS course provided by the University of Tokyo, and the Fellowship for Integrated Materials Science and Career Development provided by the Japan Science and Technology Agency. C.C. acknowledges support through a postdoctoral fellowship by the Tin Ka Ping Foundation. Q.-F.L. further acknowledges support from the computational resource of Fujitsu PRIMERGY CX2550M5/CX2560M5 (Oakbridge-CX) awarded by the “Large-scale HPC Challenge” Project, Information Technology Center, The University of Tokyo, for the Monte Carlo simulation.

S. S., J. Z., and Y. H. L. grew the thin-film samples under the supervision of C. C. R. L. carried out the electrical transport measurements. C. Z., X. G., and R. Y. carried out the tight-binding model and DFT calculations. Q. F. L. and X. Z. carried out the Monte Carlo simulations. K. Q. fabricated the Hall bar devices. S. S., R. L., and C. Z. analyzed the data. B. J. conceived the study. B. J., Q. S., K. T. L., and Z. Y. M. supervised the study. All authors discussed the results and contributed to the manuscript, which was written by B. J.

[1] R. Karplus and J. M. Luttinger, *Hall effect in ferromagnetics*, *Phys. Rev.* **95**, 1154 (1954).

- [2] F. D. M. Haldane, *Berry curvature on the Fermi surface: Anomalous Hall effect as a topological Fermi-liquid property*, *Phys. Rev. Lett.* **93**, 206602 (2004).
- [3] N. Nagaosa, J. Sinova, S. Onoda, A. H. MacDonald, and N. P. Ong, *Anomalous Hall effect*, *Rev. Mod. Phys.* **82**, 1539 (2010).
- [4] E. Liu *et al.*, *Giant anomalous Hall effect in a ferromagnetic kagome-lattice semimetal*, *Nat. Phys.* **14**, 1125 (2018).
- [5] Q. Wang, Y. Xu, R. Lou, Z. Liu, M. Li, Y. Huang, D. Shen, H. Weng, S. Wang, and H. Lei, *Large intrinsic anomalous Hall effect in half-metallic ferromagnet  $\text{Co}_3\text{Sn}_2\text{S}_2$  with magnetic Weyl fermions*, *Nat. Commun.* **9**, 1 (2018).
- [6] L. Ye *et al.*, *Massive Dirac fermions in a ferromagnetic Kagome metal*, *Nature (London)* **555**, 638 (2018).
- [7] C.-Z. Chang *et al.*, *Experimental observation of the quantum anomalous Hall effect in a magnetic topological insulator*, *Science* **340**, 167 (2013).
- [8] M. Serlin, C. L. Tschirhart, H. Polshyn, Y. Zhang, J. Zhu, K. Watanabe, T. Taniguchi, L. Balents, and A. F. Young, *Intrinsic quantized anomalous Hall effect in a moiré heterostructure*, *Science* **367**, 900 (2020).
- [9] Y. Deng, Y. Yu, M. Z. Shi, Z. Guo, Z. Xu, J. Wang, X. H. Chen, and Y. Zhang, *Quantum anomalous Hall effect in intrinsic magnetic topological insulator  $\text{MnBi}_2\text{Te}_4$* , *Science* **367**, 895 (2020).
- [10] I. Sodemann and L. Fu, *Quantum nonlinear Hall effect induced by Berry curvature dipole in time-reversal invariant materials*, *Phys. Rev. Lett.* **115**, 216806 (2015).
- [11] H. Liu, J. Zhao, Y. X. Huang, W. Wu, X. L. Sheng, C. Xiao, and S. A. Yang, *Intrinsic second-order anomalous Hall effect and its application in compensated antiferromagnets*, *Phys. Rev. Lett.* **127**, 277202 (2021).
- [12] C. P. Zhang, X. J. Gao, Y. M. Xie, H. C. Po, and K. T. Law, *Higher-order nonlinear anomalous Hall effects induced by Berry curvature multipoles*, *Phys. Rev. B* **107**, 115142 (2023).
- [13] Q. Ma *et al.*, *Observation of the nonlinear Hall effect under time-reversal-symmetric conditions*, *Nature (London)* **565**, 337 (2018).
- [14] K. Kang, T. Li, E. Sohn, J. Shan, and K. F. Mak, *Nonlinear anomalous Hall effect in few-layer  $\text{WTe}_2$* , *Nat. Mater.* **18**, 324 (2019).
- [15] M. Huang *et al.*, *Intrinsic nonlinear Hall effect and gate-switchable Berry curvature sliding in twisted bilayer graphene*, *Phys. Rev. Lett.* **131**, 066301 (2023).
- [16] M. Kang *et al.*, *Dirac fermions and flat bands in the ideal kagome metal  $\text{FeSn}$* , *Nat. Mater.* **19**, 163 (2020).
- [17] B. C. Sales, J. Yan, W. R. Meier, A. D. Christianson, S. Okamoto, and M. A. McGuire, *Electronic, magnetic, and thermodynamic properties of the kagome layer compound  $\text{FeSn}$* , *Phys. Rev. Mater.* **3**, 114203 (2019).
- [18] W. R. Meier, M.-H. Du, S. Okamoto, N. Mohanta, A. F. May, M. A. McGuire, C. A. Bridges, G. D. Samolyuk, and B. C. Sales, *Flat bands in the CoSn-type compounds*, *Phys. Rev. B* **102**, 075148 (2020).
- [19] M. Kang *et al.*, *Topological flat bands in frustrated kagome lattice  $\text{CoSn}$* , *Nat. Commun.* **11**, 4004 (2020).
- [20] C. Chen, J. Zheng, R. Yu, S. Sankar, K. T. Law, H. C. Po, and B. Jäck, *Visualizing the localized electrons of a kagome flat band*, *Phys. Rev. Res.* **5**, 043269 (2023).

- [21] B. C. Sales, W. R. Meier, D. S. Parker, L. Yin, J. Q. Yan, A. F. May, S. Calder, A. A. Aczel, Q. Zhang, and H. Li, *Flat-band itinerant antiferromagnetism in the kagome metal  $\text{CoSn1-XInx}$* , arXiv:2201.12421.
- [22] L. Ye *et al.*, *A flat band-induced correlated kagome metal*, *Nat. Phys.* **20**, 610 (2024).
- [23] L. O. Vogt, T. Ericsson, R. Wüppling, and K. Chandra, *Studies of the magnetic structure of FeSn using the Mössbauer effect*, *Phys. Scr.* **11**, 47 (1975).
- [24] Y. Xie, L. Chen, T. Chen, Q. Wang, Q. Yin, J. R. Stewart, M. B. Stone, L. L. Daemen, E. Feng, and H. Cao, *Spin excitations in metallic kagome lattice FeSn and CoSn*, *Commun. Phys.* **4**, 1 (2021).
- [25] H. Inoue, M. Han, L. Ye, T. Suzuki, and J. G. Checkelsky, *Molecular beam epitaxy growth of antiferromagnetic kagome metal FeSn*, *Appl. Phys. Lett.* **115**, 72403 (2019).
- [26] See Supplemental Material at <http://link.aps.org/supplemental/10.1103/PhysRevX.14.021046> for information on the structural and chemical sample characterization, additional experimental data to support the conclusions of this manuscript, as well as details of theoretical model calculations.
- [27] B. Stenstrom, *The electrical resistivity of FeSn single crystals*, *Phys. Scr.* **6**, 214 (1972).
- [28] Y. Gao, S. A. Yang, and Q. Niu, *Field induced positional shift of Bloch electrons and its dynamical implications*, *Phys. Rev. Lett.* **112**, 166601 (2014).
- [29] H. M. Guo and M. Franz, *Topological insulator on the kagome lattice*, *Phys. Rev. B* **80**, 113102 (2009).
- [30] X. Zhang, K. Sun, and Z. Y. Meng, *The “sign problem” of the 3rd order anomalous Hall effect in topological magnetic materials*, arXiv:2303.00819.
- [31] J. Smit, *The spontaneous Hall effect in ferromagnetics I*, *Physica* **21**, 877 (1955).
- [32] J. Smit, *The spontaneous Hall effect in ferromagnetics II*, *Physica* **24**, 39 (1958).
- [33] L. Berger, *Side-jump mechanism for the Hall effect of ferromagnets*, *Phys. Rev. B* **2**, 4559 (1970).
- [34] C. Dames and G. Chen,  *$1\omega$ ,  $2\omega$ , and  $3\omega$  methods for measurements of thermal properties*, *Rev. Sci. Instrum.* **76**, 124902 (2005).
- [35] X. Huang, C. Guo, C. Putzke, J. Diaz, K. Manna, C. Shekhar, C. Felser, and P. J. W. Moll, *Non-linear Shubnikov-de Haas oscillations in the self-heating regime*, *Appl. Phys. Lett.* **119**, 224101 (2021).
- [36] Y. Tian, L. Ye, and X. Jin, *Proper scaling of the anomalous Hall effect*, *Phys. Rev. Lett.* **103**, 087206 (2009).
- [37] S. Lai *et al.*, *Third-order nonlinear Hall effect induced by the Berry-connection polarizability tensor*, *Nat. Nanotechnol.* **16**, 869 (2021).
- [38] A. Gao *et al.*, *Quantum metric nonlinear Hall effect in a topological antiferromagnetic heterostructure*, *Science* **381**, 181 (2023).
- [39] N. Wang *et al.*, *Quantum-metric-induced nonlinear transport in a topological antiferromagnet*, *Nature (London)* **621**, 487 (2023).
- [40] K. Takahashi, J. Shiogai, H. Inoue, S. Ito, S. Kimura, S. Awaji, and A. Tsukazaki, *Single-domain formation of SrMnBi<sub>2</sub> films on polar LaAlO<sub>3</sub> substrate*, *AIP Adv.* **10**, 105216 (2020).
- [41] A. Szytula, W. Baela, L. Gondek, T. Jaworska-Gol, B. Penc, N. Stüsser, and A. Zygmunt, *Neutron diffraction and magnetisation studies of magnetic ordering in RAuIn (R = Tb, Dy, Ho)*, *J. Alloys Compd.* **336**, 11 (2002).
- [42] Y. Tang *et al.*, *Simulation of Hubbard model physics in WSe<sub>2</sub>/WS<sub>2</sub> moiré superlattices*, *Nature (London)* **579**, 353 (2020).
- [43] Y. Xu *et al.*, *Coexisting ferromagnetic–antiferromagnetic state in twisted bilayer CrI<sub>3</sub>*, *Nat. Nanotechnol.* **17**, 143 (2021).
- [44] J. A. Sears, M. Songvilay, K. W. Plumb, J. P. Clancy, Y. Qiu, Y. Zhao, D. Parshall, and Y. J. Kim, *Magnetic order in  $\alpha$ -RuCl<sub>3</sub>: A honeycomb-lattice quantum magnet with strong spin-orbit coupling*, *Phys. Rev. B* **91**, 144420 (2015).
- [45] Y. Kasahara *et al.*, *Majorana quantization and half-integer thermal quantum Hall effect in a Kitaev spin liquid*, *Nature (London)* **559**, 227 (2018).
- [46] Y. Fang, J. Cano, S. Ali, and A. Ghorashi, *Quantum geometry induced nonlinear transport in altermagnets*, arXiv:2310.11489.
- [47] C. Sürgers, G. Fischer, P. Winkel, and H. V. Löhneysen, *Large topological Hall effect in the non-collinear phase of an antiferromagnet*, *Nat. Commun.* **5**, 1 (2014).
- [48] X. Cao *et al.*, *Giant nonlinear anomalous Hall effect induced by spin-dependent band structure evolution*, *Phys. Rev. Res.* **4**, 023100 (2022).
- [49] Z. Feng *et al.*, *An anomalous Hall effect in altermagnetic ruthenium dioxide*, *National electronics review* **5**, 735 (2022).
- [50] A. K. Nayak *et al.*, *Large anomalous Hall effect driven by a nonvanishing Berry curvature in the noncollinear antiferromagnet Mn<sub>3</sub>Ge*, *Sci. Adv.* **2**, e1501870 (2016).
- [51] L. Šmejkal, A. H. MacDonald, J. Sinova, S. Nakatsuji, and T. Jungwirth, *Anomalous Hall antiferromagnets*, *Nat. Rev. Mater.* **7**, 482 (2022).
- [52] S. Nakatsuji, N. Kiyohara, and T. Higo, *Large anomalous Hall effect in a non-collinear antiferromagnet at room temperature*, *Nature (London)* **527**, 212 (2015).
- [53] D. Hong, C. Liu, H.-W. Hsiao, D. Jin, J. E. Pearson, J.-M. Zuo, and A. Bhattacharya, *Molecular beam epitaxy of the magnetic kagome metal FeSn on LaAlO<sub>3</sub> (111)*, *AIP Adv.* **10**, 105017 (2020).
- [54] S. Cheng, B. Wang, I. Lyalin, N. Bagueés, A. J. Bishop, D. W. McComb, and R. K. Kawakami, *Atomic layer epitaxy of kagome magnet Fe<sub>3</sub>Sn<sub>2</sub> and Sn-modulated heterostructures*, *APL Mater.* **10**, 061112 (2022).
- [55] D. Kumar, C. H. Hsu, R. Sharma, T. R. Chang, P. Yu, J. Wang, G. Eda, G. Liang, and H. Yang, *Room-temperature nonlinear Hall effect and wireless radiofrequency rectification in Weyl semimetal TaIrTe<sub>4</sub>*, *Nat. Nanotechnol.* **16**, 421 (2021).
- [56] L. Miao, R. Du, Y. Yin, and Q. Li, *Anisotropic magneto-transport properties of electron gases at SrTiO<sub>3</sub> (111) and (110) surfaces*, *Appl. Phys. Lett.* **109**, 261604 (2016).
- [57] S. McKeown Walker, A. De La Torre, F. Y. Bruno, A. Tamai, T. K. Kim, M. Hoescher, M. Shi, M. S. Bahramy, P. D. C. King, and F. Baumberger, *Control of a two-dimensional electron gas on SrTiO<sub>3</sub> (111) by atomic oxygen*, *Phys. Rev. Lett.* **113**, 177601 (2014).